

Combinatorial Block Copolymer Ordering on Tunable Rough Substrates

Manish M. Kulkarni,[†] Kevin G. Yager,[‡] Ashutosh Sharma,[§] and Alamgir Karim^{*,†}

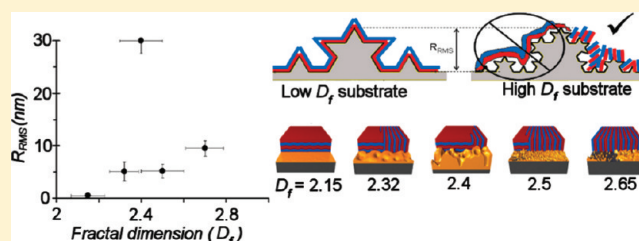
[†]Department of Polymer Science and Polymer Engineering, Akron Functional Materials Center, The University of Akron, Akron, Ohio 44325, United States

[‡]Center for Functional Nanomaterials, Brookhaven National Laboratory, Upton, New York 11973, United States

[§]Department of Chemical Engineering, Indian Institute of Technology, Kanpur, Kanpur, UP 208016 India

S Supporting Information

ABSTRACT: Morphology control of block copolymer (BCP) thin films through substrate interaction via controlled roughness parameters is of significant interest for numerous high-tech applications ranging from solar cells to high-density storage media. While effects of substrate surface energy (SE) and roughness (R) on BCP morphology have been individually investigated, their synergistic effects have not been explored in any systematic manner. Interestingly, orientation response of BCP to changes in SE can be similar to what can be accomplished with variations in R . Here we present a novel approach for orienting lamellar BCP films of poly(styrene)-*block*-poly(methyl methacrylate) (PS-PMMA) on spin-coated xerogel (a dried gel of silica nanoparticle network) substrate with simultaneously tunable surface energy, $\gamma_s \sim 29$ –53 mJ/m², by UVO exposure and roughness, $R_{\text{rms}} \sim 0.5$ –30 nm, by sol–gel processing steps of regulating the catalyst concentration and sol aging time. As in previous BCP orientation studies on 20 nm diameter monodisperse silica nanoparticle coated surface, we find a similar but broadened oscillatory BCP orientation behavior with film thickness due to the random rather than periodic rough surfaces. We also find that higher random roughness amplitude is not the necessary criteria for obtaining a vertical orientation of BCP lamellae. Rather, a high surface fractal dimension ($D_f > 2.4$) of the rough substrate in conjunction with an optimal substrate surface energy $\gamma_s \sim 29$ mJ/m² results in 100% vertically oriented lamellar microdomains. The AFM measured film surface microstructure correlates well with the internal 3D BCP film structure probed by grazing incidence small-angle X-ray scattering (GISAXS) and rotational small-angle neutron scattering (SANS). In contrast to tunable self-assembled monolayer (SAM)-coated substrates, the xerogel films are very durable and retain their chemical properties over period of several months. These results also highlight importantly that BCP orientation control for nanotechnology is possible not only on specially prepared patterned substrates but also on industrially viable sol–gel substrates.



1. INTRODUCTION

Rough substrates are used in various scientific and technological applications such as superhydrophobic and oleophobic surfaces,^{1–3} controlled dewetting of polymer films⁴ and liquid crystal ordering,⁵ controlled adhesive properties of surfaces,⁶ and for cell growth.⁷ The nature of roughness can be periodic or nonperiodic, although some of the nonperiodic substrates exhibit a “surface pattern” associated with a dominant wavelength. The response of various material coatings and self-assembling systems on periodic patterns has been the subject of a vast number of studies in the past decade.^{8,9} However, by comparison, the response of thin films and coatings on nonperiodic rough surfaces has been relatively less studied due to difficulties in reproducible control of surface roughness. In addition to the surface roughness, controlling the surface energy of the substrates for adhesion and stability of the coatings against dewetting or to obtain preferential morphology of the polymer films is imperative. Of significant interest then is how the synergy of interaction provided by well-characterized random or aperiodic surface roughness and concurrent surface

energy effects structural changes to self-assembling thin film coatings such as block copolymers (BCPs). Here we first demonstrate a versatile sol–gel method to create aperiodic rough substrates with high reproducibility of roughness and surface energy. We use the functionality provided by these novel substrates to demonstrate control over orientation of lamellar BCP phases in thin films.

Self-assembly of BCPs has gained recent importance in nanopatterning where relatively simple large-area patterns are required (e.g., hard disk drive patterning) or low-cost, low-fidelity patterning is needed (e.g., organic photovoltaics).¹⁰ It can also serve as an alternative to the high resolution patterning needs of semiconductor industry,¹¹ where lithography puts severe limits on the materials that can be used for creating nanostructures.¹² Therefore, there is an immediate need for developing alternate low-cost and generic methods that are also

Received: January 23, 2012

Revised: April 6, 2012

Published: May 1, 2012

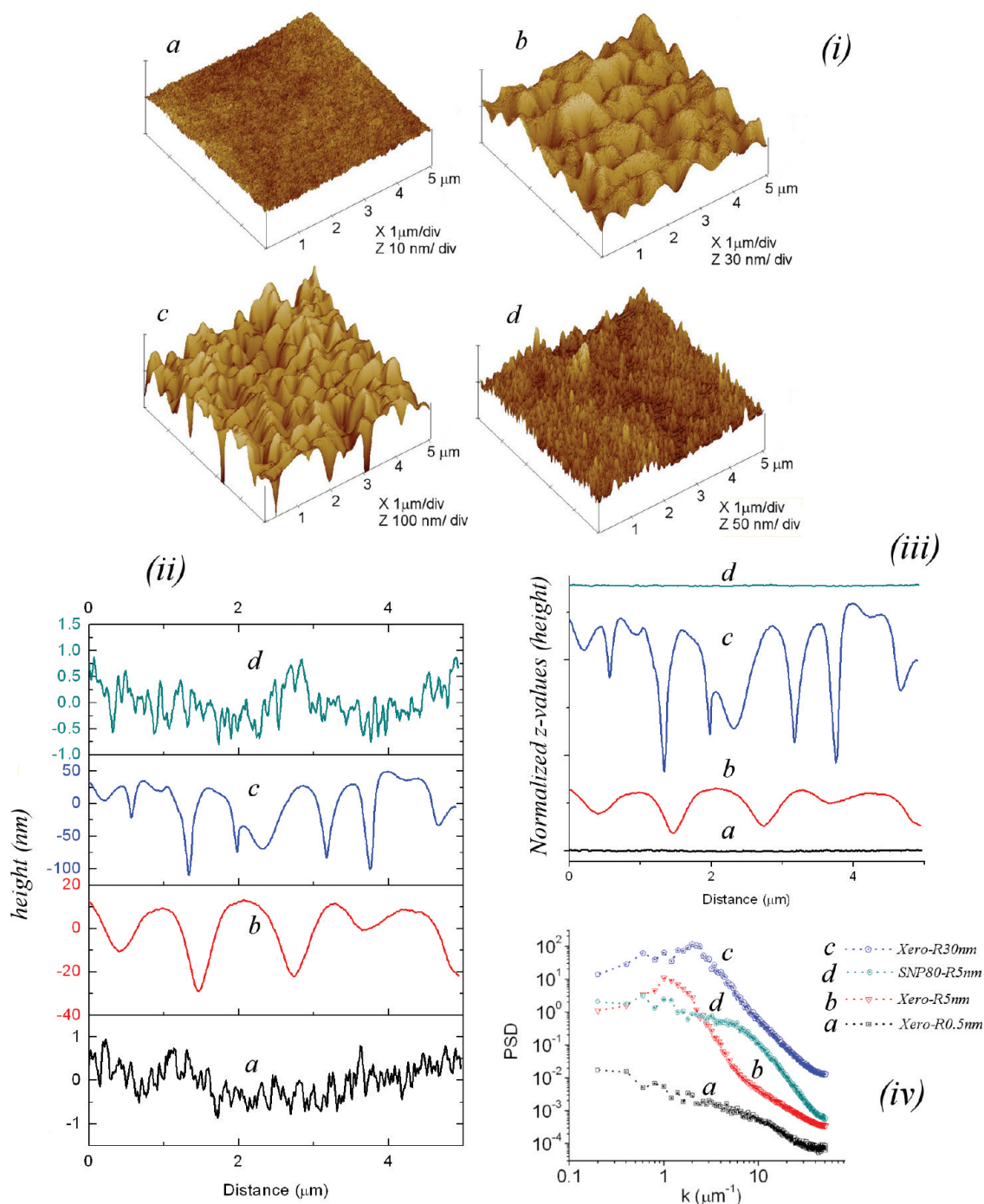


Figure 1. (i) AFM 3D topographic images of substrates used to coat the BCP films: (a) Xero-R0.5 nm, $R_{\text{rms}} = 0.5 (\pm 0.2)$ nm; (b) Xero-R5 nm, $R_{\text{rms}} = 5.1 (\pm 1.8)$ nm; (c) Xero-R30 nm, $R_{\text{rms}} = 30.4 (\pm 2.4)$ nm; and (d) silica nanoparticle layer coated on silicon substrate ($\approx 80\%$ coverage) SNP80-R5 nm, $R_{\text{rms}} = 5.2 (\pm 1.3)$ nm. (ii) Typical line cross section of AFM topograph for all the substrates. (iii) The smoothness of substrates a and d compared to b and c can be appreciated easily in normalized z-scale. (iv) 2-D isotropic power spectral density plots obtained from the height image. PSD of samples b and c suggest presence of a dominant periodicity indicated by a peak.

capable of producing defect-free and patterned nanoscale structures over large areas. Self-assembly of BCPs¹³ is one of the most promising of the emerging technologies¹⁴ for soft nanopatterning. The range of phase structures exhibited by BCPs makes it an attractive technique to create nanoscale features of different shapes like sphere, rod (cylinder), lamellae, and gyroid.¹⁵ Although it has already been demonstrated that cylindrical BCP thin films can be used for high-density data storage devices,^{16,17} there are significant challenges in similarly

using lamellar BCP since usually one of the blocks of lamellar BCP preferentially wets the substrate, and consequently, the majority of lamellae lie horizontal or parallel to the plane of the substrate.^{18,19} However, the use of BCP in nanopatterning applications requires that the lamellae orient perpendicularly (vertically) to the substrate so that typically one of the blocks can be selectively etched out^{20,21} to obtain parallel grating-like lines over a large area. We report on this challenge of controlling orientation of lamellar BCP domains with the help

Table 1. Surface Properties of the Rough Substrates

substrate	roughness R_{rms} (nm) ^a	dominant λ (μm)	qR_{rms} ^b	fractal dimension D_f ^a
Xero-R0.5 nm	0.5 (± 0.2)			2.15 (± 0.08)
Xero-R5 nm	5.1 (± 1.8)	0.99	0.03	2.32 (± 0.07)
Xero-R30 nm	30.4 (± 2.4)	0.5	0.38	2.4 (± 0.1)
SNP80-R5 nm	5.2 (± 1.3)	1.6	0.019	2.5 (± 0.1)

^aEstimated errors are standard deviation of three different measurements. ^b $q = 2\pi/\lambda$.

of the tunable rough substrates based on the sol–gel method mentioned earlier.

In order to obtain vertically oriented lamellar BCP domains, several approaches have been proposed including chemical patterning and/or modification of the substrate,^{22–24} sandwiching the BCP between two neutral surfaces,²⁵ addition of nanoparticles to the polymer films,^{26,27} coating the BCP films on rough substrates,²⁸ and addition of surfactant molecules.²⁹ The addition of nanoparticles or surfactants to the BCP film introduces an unwanted third component in the film, and the chemical and topographic substrate modification techniques require pre patterning of the substrate (chemical and/or physical) on a length scale of the order of L_0 (the BCP repeat spacing), which is of the order of tens of nanometers.⁸ It is also noteworthy that the BCP nanopatterns are attractive precisely because of the self-assembly of the structures. While using a periodic nano- or micropatterned substrate may add precision in nanopatterning, it loses much of the advantage of the self-assembly process, and further the BCP pattern is limited by the area of the pre patterned substrate. Our sol–gel substrate bypasses these problems and also allows for a fundamental study of how roughness and surface energy synergistically combine to impact BCP orientation.

2. EXPERIMENTAL SECTION

Substrate and Film Preparation. Two methods were used to prepare the substrates before coating the BCP films on them. First, a two-step acid–base catalyzed sol–gel polymerization method reported previously to prepare bulk silica xerogels was modified and used to prepare silica xerogel thin films of different surface features.³⁰ Briefly, ethanol (EtOH) diluted tetraethoxysilane (TEOS) (Fluka, purum 98%) solution was mixed with propyltrimethoxysilane (PrTMS) (Aldrich, 97%) hydrophobic reagent. Then aqueous hydrochloric acid (HCl, volume fraction 2%) was added in this mixture such that the molar ratio of TEOS:EtOH:PrTMS:H₂O (added to dilute HCl) was around 1:6.9:0.18:3.2, respectively. The mixture was homogenized by shaking using an autoshaker for 15 min, and this solution was used as stock after aging it for ≈ 24 h. The final silica sol was prepared by mixing the stock solution with aqueous ammonium hydroxide (NH₄OH) solution of different molarities from 0.1 to 0.5 mol/L such that the TEOS:H₂O (added to dilute NH₄OH) molar ratio was about 1:2.2. Prior to the gelation point, the sol was aged for different time periods from 0 to 30 min (counted from NH₄OH addition) before spin-coating it on polished silicon wafers. Spin-coating was performed at 209 rad/s (2000 rpm) for 60 s. The films were then dried under atmospheric pressure at 130 °C for about 12 h to remove any residual solvent. Additionally, silicon substrates were also coated by silica nanoparticle by slightly modifying a process reported previously³¹ such that the layer of nanoparticles covered most of the surface ($\approx 80\%$ area fraction as determined by AFM). For this dispersion (volume fraction 0.2%) of propyl-terminated silica nanoparticles (≈ 20 nm diameter) in chloroform was spin-coated on polished and cleaned silicon wafers at 209 rad/s (2000 rpm) for 60 s. These films were dried at room temperature for 1 h so that the volatile chloroform evaporated before using them for further processing. The topography of all the films was studied by AFM by scanning $5\ \mu\text{m} \times 5\ \mu\text{m}$ areas at three different locations, and four films (see Figure 1)

were selected based on the difference in their surface features, as depicted in Table 1, to coat the BCP films.

In order to generate a surface energy gradient, each of the selected substrate silica films was placed on an accelerating stage. This stage was accelerated such that different sections of the sample were exposed to UV-ozone (UVO) for different amount of time by passing the sample under UV-wand (185 and 254 nm wavelength). Radiation power varied from 5 to 700 mJ/cm², depending upon exposure time.³² The surface energy gradient was determined by Owen's method by measuring sessile drop (3 μL) contact angles (Kruss DSA 100 contact angle goniometer) of toluene, water, and diiodomethane on xerogel substrates.³³ Fractal dimension (D_f) of the substrates was measured from the AFM topography images using a box-counting method.¹⁹ A cube lattice with lattice constant L was superimposed on the 512 pixel by 512 pixel topographic scan of the substrate. The surface area is obtained by multiplying number of cubes that contain at least 1 pixel by L^2 . This procedure was repeated by changing L from 1 to 512, and the fractal dimension was extracted from the scaling of this box count with L . In the next step, deuterated poly(styrene)-*block*-poly(methyl methacrylate) (PS-PMMA) (Polymer Source, Inc., polydispersity index = 1.14) with PS $M_w = 29.5$ kg/mol and PMMA $M_w = 33.1$ kg/mol was dissolved in toluene (Sigma-Aldrich). This solution (BCP weight fraction 0.03) was flow-coated on the UVO-exposed substrate fixed on an accelerating stage to obtain films with either constant or gradient thickness.³⁴ Specifically, a 50 μL drop of the polymer solution was placed at a wedge between a glass plate held at fixed angle and the substrate, and the stage was accelerated from 1 to 10 mm/s² with terminal velocities from 3 to 12 mm/s, depending on desired thickness gradient. Uniformly thick films were obtained at higher acceleration of 160 mm/s². All the films were then annealed in vacuum oven for 15 h at 165 °C whereupon the BCP microphase separates.

BCP Film Characterization. Three different techniques, namely AFM phase imaging, rotational small-angle neutron scattering (R-SANS), and grazing incidence small-angle X-ray scattering (GISAXS), were used to characterize the microphase-separated BCP films. Dimension 3100 (Veeco Instruments) was used in “tapping” mode to record the topography and phase images of the films. Film thickness was measured by AFM scratch-height analysis. For the lamellae orientation analysis, the phase and amplitude images were segmented by software methods into regions of parallel and perpendicular lamellae as described in ref 31. R-SANS experiments were performed using the NG7-SANS instrument at the NIST Centre for Neutron Research, using an incident neutron beam of wavelength $\lambda = 0.6$ nm ($\Delta\lambda/\lambda = 0.11$). Uniform thickness BCP samples were spin-coated on xerogel and SiNP80 substrates and annealed in a vacuum oven. Scans were performed as a function of sample rotation angle in the range -84° to $+84^\circ$ in 4° increments. The data were normalized and rotated into a sample-aligned coordinate system as described previously.³¹ Briefly, the RSANS data were interpolated using Delaunay triangulation. This procedure effectively assumes that the orientation distribution is smooth, without variations smaller than the 4 deg step size selected for the experiment. We note that on a series of BCP test samples with different orientation distributions, we measured using a step size of 0.5 deg and saw no evidence of variation over these small tilts.

Grazing small-angle X-ray scattering (GISAXS) measurements were performed at Argonne's Advanced Photon Source using the 8-ID-E beamline. Two-dimensional scattering images were measured using charge-coupled device (CCD) detector at a distance of 1.945 m and an X-ray wavelength of 0.169 nm (photon energy of 7.35 keV). Samples

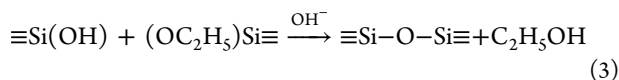
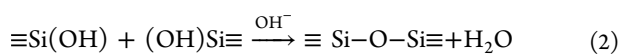
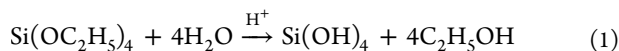
were measured under vacuum at incident angles both above (0.2°) and below (0.15°) the polymer–air critical angle, which was determined using an X-ray reflectivity scan.

3. RESULTS AND DISCUSSION

In this section we will present results and discussion on two topics. The first is the Xerogel Substrate Fabrication Chemistry and Characterization, and the second is the Lamellar PS–PMMA Orientation on Xerogel Substrates. Briefly, the tunable silica xerogel substrates used in this study were prepared by a novel and versatile sol–gel based method. Xerogel is obtained by drying a hydrogel (water-rich gel) or alcogel (alcohol-rich gel) under ambient pressure but at or above room temperature. The advantage of this sol–gel processing technique is that the silica xerogel network is a self-assembled structure requiring no external control for the preparation of large area substrates by spin or flow coating the sol. As will be discussed below, it was also observed that vertically oriented BCP patterns can be obtained over large area on these substrates with appropriate tuning of the substrate roughness and surface energy.

a. Xerogel Substrate Fabrication Chemistry and Characterization. The new sol–gel based technique was developed for preparing rough silica xerogel substrates of different characteristics is described in the Experimental Section. In order to compare with previous results, we also prepared rough substrates by spin-coating a layer of propyl-decorated silica nanoparticles (≈ 20 nm diameter) onto silicon wafers. To control the surface energy, the xerogel surface was modified using propyltrimethoxysilane (PrTMS) as a UVO-sensitive coprecursor. Figure 1 shows the 3D surface topography and power spectral density (PSD) plots of these substrates. Various surface physical properties of these rough substrates measured from AFM images are listed in Table 1.

The xerogel films were relatively thick (≈ 2 – 3 μm) by design and did not leave any exposed area of the flat silicon substrate (Figure 1a–c), whereas the average thickness of the nanoparticle layer was ≈ 20 nm, which corresponds to a nanoparticle monolayer (Figure 1d) that covered about 80% of substrate (silicon) surface area. However, few patches of the nanoparticle layer were thicker and indicated sporadic clustering and nonuniform packing of particles. We first describe here the xerogel formation and structure control along with chemical modifications observed in the xerogel films. Tetraethoxysilane (TEOS), which is the main silica precursor, hydrolyzes faster in the presence of H^+ ions and substoichiometric amount of H_2O upon addition of acidic water (aqueous solution of HCl). Most of the ethoxy groups of TEOS hydrolyze, and silicic acid ($\text{Si}(\text{OH})_4$) is produced as a result of reaction of water with TEOS in the presence of H^+ ions as shown in reaction 1:



The silica network polymerization is very slow after addition of HCl, and the solution retains its fluidity and low viscosity due to substoichiometric water and slow condensation rates of $\text{Si}-\text{OH}$ groups in acidic conditions. The polycondensation of $-\text{Si}-\text{OH}$ and $-\text{Si}-(\text{OC}_2\text{H}_5)$ groups shown in reactions 2 and 3 takes place much more quickly in the presence of OH^- ions

upon addition of base catalyst (NH_4OH) and a 3D network of silica particles starts to develop.³⁵ During the sol aging, the size of the silica particles increases initially before the cross-linking of the particles dominates the process. The cross-linking of particles leads to an increase in viscosity of the sol. Thus, by controlling the catalyst concentration as well as sol aging time, the size of the clusters forming the silica network can be tuned, which effectively determines the final roughness of the xerogel substrate. The particle size and viscosity of the sol increased with increase in the aging time and/or NH_4OH concentration, and its effect on the xerogel substrate topography was studied by AFM. As the silica network formation begins after addition of NH_4OH , the viscosity of the sol starts to increase with time and at the gel point the sol ceases to flow. In a primary experiment, gelation period was noted for bulk sol in a mold. Thin silica xerogel films were prepared by spin-coating the sol on Si wafers before the gelation time, when sol was still in liquid state. The solvent evaporation during spin-coating process leads to quicker gelation of silica films that gelled almost immediately.

The topography of xerogel films (sample Xero-R0.5 nm) synthesized using 0.1 M NH_4OH with sol aging time of 15 min (Figure 1(i)a) shows that the film surface is very smooth, mainly composed of very small (<20 nm) silica nanoparticles, and the measured xerogel surface rms roughness (~ 0.5 nm) is even smaller due to the close packing of silica clusters. Moreover, the power spectral density (PSD), which is an isotropic fast Fourier transform (FFT) of the local height data, does not show any dominant wavelength, as expected for such smooth surfaces. Note that the clusters forming silica xerogel network are about the same size as that of AFM tip radius (≈ 20 nm), so for a $5\text{ }\mu\text{m}^2$ area scan with 512 pixels/line, the AFM image cannot resolve these clusters very well, which explains absence of any dominant peak around 20 nm wavelength in PSD. When the NH_4OH concentration was increased to 0.2 M, the viscosity of the sol increased and the particle size increased to ≈ 50 nm. Figure 1(i)b shows the surface topography of a substrate, Xero-R5 nm, coated immediately after addition of 0.2 M NH_4OH . Figure 1(i)c shows the surface of another sample, Xero-R30 nm, which is coated after aging the sol for 7 min. It is seen that both of these surfaces have higher roughness than Xero-R0.5 nm. Higher aging time results in bigger particle size and loosely packed network, which in turn also increases the void sizes in the network. Also, due to the faster cross-linking of the particles at higher NH_4OH concentrations, the gelation is very fast and a higher quantity of solvent remains trapped in the pores of the gel after spin-coating, as compared to gels with lower NH_4OH concentration. When the gel films were dried in the oven, bubbling evaporation of the solvent leads to formation of larger pores in the film. This formation of larger particles and pores increases the roughness of these films. From the AFM topography cross section of all samples shown in Figure 1(ii) it is clear that Xero-R5 nm showed pores of depth <30 nm depth, whereas for Xero-R30 nm, the pores were ≈ 100 nm deep. In comparison, the other two substrates used in this study were very smooth as seen from the normalized cross section in Figure 1(iii) and shown an overall height variation <5 nm. Another important feature that might show up for some of the rough surfaces is the presence of dominant surface pattern. Here, the PSD analysis from AFM topography shown in Figure 1(iv) shows that only PSD of samples Xero-R5 nm and Xero-R30 nm suggest the presence of a dominant self-organized periodicity in the topography around 2 and 3 μm , respectively,

which can be attributed to the nonuniform bigger silica clusters and pores.

Figure 1(i)d shows the surface topography of the sample SNP80-R5 nm created by coating silica nanoparticles (≈ 20 nm diameter) on Si wafer. Apart from a few clustered and uncoated regions, the nanoparticles formed a monolayer on the Si wafer and covered about 80% of the area. The surface exhibits bimodal periodicity, and the dominant wavelength observed around $2\ \mu\text{m}$ in PSD is related to the island formation of nanoparticles. Three different regions of each of the samples were scanned by AFM, and the root-mean-square (rms) roughness R_{rms} , PSD, and fractal dimension (D_f) data were collected, and their average values are listed in Table 1. The clustering and island formation of nanoparticles in the SNP80-R5 nm substrates, as well as the pore sizes in the xerogel substrates, strongly influenced the dominant wavelength in the PSD analysis. As such, the calculated qR_{rms} may not represent the roughness which is most relevant to a given self-assembly (e.g., the dominant wavelength may be irrelevant at the size scale of BCP assembly as discussed later). These results thus further underline the need for alternative methods to characterize the rough substrates. One of the parameters that defines roughness of the given surface is fractal dimension (D_f), which is a measure of the space occupying capacity of the surface in the third dimension and can be thought of as the “texture” of a given roughness. In order to characterize the random or aperiodic surface roughness in terms of D_f and its potential effect on BCP ordering, we provide a brief introduction here. $D_f = 2$ is a precisely two-dimensional surface lacking any scale-dependent surface features (e.g., an absolutely smooth surface with no asperities), whereas a surface with D_f closer to a value of 3 has multiscale surface irregularities (e.g., a highly porous surface or one with asperities at all size scales). The texture of a given surface is simple at low D_f as compared to complex and irregular for larger D_f .

With $D_f \approx 2.5$, the SNP80-R5 nm was the surface with the highest fractal dimension, even though its $R_{\text{rms}} \approx 5.2$ nm was significantly lower than Xero-R30 nm ($R_{\text{rms}} \approx 30$ nm, $D_f \approx 2.4$) and nearly the same as that of Xero-R5 nm ($R_{\text{rms}} \approx 5.1$ nm, $D_f \approx 2.32$). It should be noted here that D_f values were consistently calculated from $5\ \mu\text{m}$ by $5\ \mu\text{m}$ AFM scans, but this parameter does vary somewhat as a function of scan size owing to the different small and long-range surface oscillations. Localized clustering of particles and other inhomogeneities in the silica xerogel and nanoparticle layers may significantly affect D_f measured over much larger areas. We selected $(5\ \mu\text{m})^2$ for measuring the D_f values because the nanoparticle and xerogel coating was homogeneous over this area, and it is very large as compared to the domain spacing L_0 of BCP films used in the present study.

b. Lamellar PS–PMMA Orientation on Xerogel Substrates. We examined the versatility of the tunable xerogel substrates in orienting lamellae forming PS–PMMA BCP as a function of film thickness h , interaction of the blocks with the substrate and substrate roughness. The roughness acts on the BCP phases through entropic chain packing conformational effects while their response to the substrate surface energy is enthalpic and selective. Experimentally, these relations do not exist for a systematic exploration of synergistic effect of surface energy and roughness over a broad range of these variables on BCP ordering. For this reason, BCP orientation on random or aperiodic rough surfaces is currently not well understood, and there are only a handful of studies that have addressed this issue

for fixed parameters of roughness with no effort to vary the native surface energy of the substrate or vice versa. For symmetric BCP films with sublamellar ($h < L_0$) thicknesses, Fasolka et al.³⁶ have shown that vertically oriented phases can be obtained for films with $h < L_0/2$ coated on rough as well as flat silicon substrates. For BCP films thicker than L_0 , Sivaniah et al.²⁸ have argued that the product of wave vector and root-mean-square (rms) roughness (at given substrate surface energy) is one of the critical parameters for rough substrates with a single dominant periodic mode. This quantity is essentially the aspect ratio of the undulation, i.e., ratio of its amplitude to its wavelength. The critical value of this parameter for perpendicular orientation of BCP lamellae was shown to be 0.4 experimentally and 0.96 for a model surface with the sinusoidal profile. This is an important result in understanding the BCP orientational response on wavy surfaces.

However, many natural and industrially relevant surfaces prepared without special patterning techniques are typically spectrally rough with randomly distributed asperities and devoid of a dominant length scale. Indeed, it is interesting to note that qR_{rms} values (Table 1) for all the surfaces used in this study are well below the critical experimental and theoretical values of 0.4 and 0.96 as reported in their studies. Hence, we tried to correlate our findings of lamellar orientation with another important property of a rough substrate, D_f , its surface fractal dimension that has been overlooked until now. As will be discussed later in this article, fractal dimension of a surface reflects its space-filling capacity in the third dimension, so a surface with lower roughness amplitude but more hierarchical asperities can have a higher fractal dimension compared to a surface with larger roughness amplitude. We correlated effect of fractal dimension of the substrate with the orientational tendency of BCP films in this paper.

Further, the possible effect of a coupling between roughness and surface energy in orienting BCP films is worthy of investigation. Addition of PrTMS to the xerogels gives a handle to control the surface energy of the xerogel substrates. PrTMS mixed as a coprecursor in the sol–gel processing stage replaces some of the $-\text{OH}$ groups on the silica cluster surface by hydrolytically stable $\text{O}-\text{Si}-(\text{C}_3\text{H}_7)_3$ groups which leads to hydrophobic xerogel surface similar to some of the other silica coprecursors used in our earlier studies on aerogels.³⁷ The $\text{Si}-(\text{C}_3\text{H}_7)_3$ groups photo-oxidize when exposed to UVO, similar to reported in ref 38. The topography or hardness of the xerogel substrate remains mostly unaffected as the covalent bonds of SiO_2 forming the xerogel structure do not dissociate by UVO exposure. We did not observe any change in the topography of the samples before and after exposing it to UVO from the AFM scans. Therefore, the surface energy of the xerogel films can be tuned as desired by controlling the UVO exposure time. The xerogel layer has very similar properties that of glass except with higher porosity and tunable surface functional groups. The UVO treatment effectively tunes the surface energy of the xerogel substrate. Because of the wide range over which we can tune surface energy, this methodology is applicable to targeting neutral or preferential wetting conditions for a wide range of block copolymers or even blends of polymers or small molecules. As such, we view this as an extremely general and generic strategy for directed assembly.

The basic understanding of orientational response of BCP films and their control on such hierarchical rough, multiscale substrates of different surface energies is of immense practical

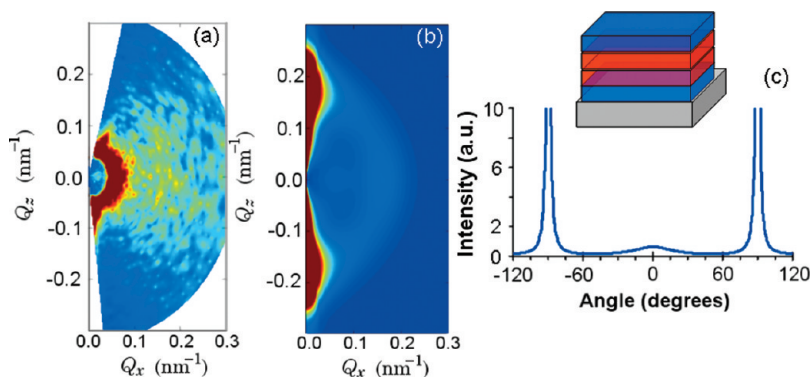


Figure 2. (a) Experimental reciprocal-space contour plot showing orientation of lamellae (a linear color, with blue being low-intensity, and red being high-intensity, is applied). Data were obtained by rotational-small angle neutron scattering (R-SANS) for a 40 nm thick BCP film coated on Xero-R0.5 nm with $\gamma_s = 29$ mJ/m². (b) Corresponding fit of the data. (c) Orientational distribution of lamellae as a function of tilt angle (0° denotes vertically oriented lamellae, whereas ±90° denotes horizontally oriented lamellae). Inset shows a schematic of parallel orientation of lamellae as indicated by the R-SANS.

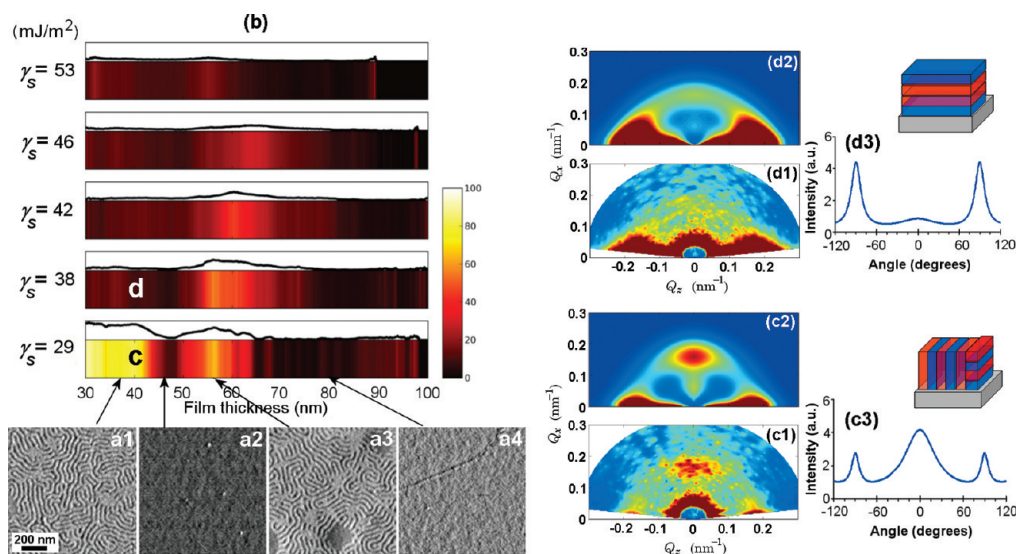


Figure 3. Plot of percentile perpendicular lamellae orientation (line plots above each color bands) as a function of the film thickness obtained by analyzing all the AFM phase images by software. Higher elevation of a point on the line corresponds to higher vertical lamellae population at the specified thickness and surface energy. The data were converted to a color band spectrum scaled as shown below the plot. Arrows indicate approximate data position on the curve obtained from the corresponding (a) AFM image (scale bar: 200 nm). (b) Color bands show percentile perpendicular lamellae distribution as a function of xerogel surface energy (γ_s) and film thickness for PS–PMMA films coated on Xero-R5 nm. (c1, d1) 2-D contour color maps in reciprocal space showing orientation of lamellae obtained by the rotational small-angle neutron scattering (R-SANS) recorded for 40 nm thick BCP films coated on Xero-R5 nm with (c) surface energy $\gamma_s = 29$ mJ/m² and (d) $\gamma_s = 38$ mJ/m². Pixel colors ranging from dark blue to dark red represent R-SANS scattering intensity from 0 to 100 (arbitrary units). (c1) and (d1) show linearly scaled experimental 2-D slices of reciprocal space obtained using R-SANS while (c2) and (d2) show the corresponding fits. (c3) and (d3) show orientational distribution of lamellae as a function of tilt angle (0° denotes vertically oriented lamellae, whereas ±90° denotes horizontally oriented lamellae). Schematic figures shows orientation of lamellae as indicated by respective R-SANS.

importance but currently poorly understood. We try to address some of these issues in the present paper.

0.5 nm Rough Xerogel Substrate. AFM was used to analyze the surface orientation of annealed BCP films coated on xerogel and SiO₂ nanoparticle coated substrates. As mentioned earlier, the surface of Xero-R0.5 nm was extremely smooth with $R_{\text{rms}} = 0.5$ nm and $D_f = 2.15$. Such a low roughness is not expected to induce a vertical orientation of lamellae. Indeed, we can conclude from absence of nanoscale phase AFM features that the BCP lamellae lie parallel on the substrates for almost all thicknesses, except on the edges of some small defects on the substrate. Figure 2 shows total film BCP ordering measured by

rotational small angle neutron scattering (R-SANS) on Xero-R0.5 nm substrate at a surface energy of $\gamma_s = 29$ mJ/m².

The net summary of information that can be gleaned from the sharp vertical peaks at ±90° in R-SANS (Figure 2c), coupled by the fit to raw scattering data in Q_z – Q_x scattering reciprocal space (Figure 2a,b) indicates absence of vertically oriented lamellae as there is barely any signal above background at 0° angle. Further, in this case even at high wafer tilt angle we did not resolve any signal from the horizontal state, though RSANS is limited in the angular range it can probe. But absence of any strong signal above zero degrees suggests a predominantly horizontally ordered system, with a fairly small angular spread as shown in the schematic in Figure 2. This

result is similar to the parallel orientation of BCP lamellae observed on low-roughness substrate (e.g., a silicon wafer) where a partially hydrophilic surface favors PMMA wetting at that interface which leads to horizontal lamellae. We can thus consider Xero-R0.5 nm as a reference densely packed ultrasmooth substrate for xerogel based studies in the future with tunable surface energy. For a smooth substrate, we anticipate that when the BCP–substrate interface is chemically near neutral conditions; i.e., when the wetting energies of both the blocks are similar, it favors vertical BCP orientation for all BCP film thicknesses.

5 nm Rough Xerogel Substrate. We processed the raw data obtained from the phase and amplitude AFM images to a false-color orientation map as shown in Figure 3 for easy to follow representation of the effect of film thickness as well as surface energy on the orientation of BCP phases. As described in the Experimental Section, the samples were prepared in 2-D combinatorial manner with variation in lamellar BCP film thickness gradient created by flow coating on the xerogel substrate with a gradient UV-ozone (UVO) exposure (surface energy), orthogonal to each other. A 2-D library of AFM images was collected as a function of substrate surface energy and BCP film thickness by scanning at periodic locations on the surface of the 2-D combinatorial sample.

The analysis process is shown in Figure 3 as an example for phase images of four scans as a function of film thickness for BCP coated on Xero-R5 nm which has $R_{\text{rms}} = 5.1$ nm, $D_f = 2.32$, and $\gamma_s = 29$ mJ/m². Using these images and amplitude data, the percentage of vertical oriented lamellae over a given area was calculated using software described in the Experimental Section. The results are shown in Figure 3b. For ease of visualization of BCP orientation response on these combinatorial samples, each γ_s (substrate surface energy) value, the orientation vs film thickness (h) plot (shown above each spectral bar) was converted to a color band spectrum where bright yellow-white indicates areas with 100% vertical orientation of lamellae, whereas deep red indicates surface areas with 0% vertically oriented lamellae (i.e., 100% parallel lamellae). Other colors represent intermediate values of fractional areas of perpendicular orientation as shown in the vertical scale bar. Figure 3b shows perpendicular orientation of lamellae for the BCP films coated on the Xero-R5 nm as a function of film thickness versus the full range of xerogel surface energy ($29 < \gamma_s < 53$) mJ/m².

An oscillation of the lamellar orientation, between horizontal and vertical, with increasing film thickness, is qualitatively observed in these scans with a damping with increasing BCP film thickness. The damped oscillatory behavior in orientation with increasing film thickness is qualitative similar to our studies on BCP ordering on monodisperse nanoparticles,³¹ except the peak widths and oscillatory damping are much broader and polydisperse by comparison. We infer the observed “broadening” as due to the lack of a fixed lateral roughness scale of the substrate as well as a broad roughness amplitude distribution contributing to the $R_{\text{rms}} = 5.1$ nm. Furthermore, by analogy to Yager et al.,³¹ the observed oscillatory behavior in orientation with a wavelength, $\lambda \sim 25$ – 35 nm, comes from the film thickness passing through alternating parallel and perpendicular. The stable configuration corresponds to lamellae that are parallel to the substrate. Parallel orientation is in the traditional sense for smooth substrates but in the context of rough substrate interfaces, it refers to conformal orientation. We observe that for all surface energies, ($29 < \gamma_s < 53$) mJ/m²,

to differing extents, with increasing h , the lamellae orientation changed periodically between parallel and perpendicular. Importantly, as pointed out previously, the period of this oscillation, as a function of film thickness, is close to the lamellae repeat period, L_0 . The vertical orientation, as measured by AFM at the top surface, evidently does not persist beyond ≈ 70 nm in all cases. This trend of periodic changes in the lamellar orientation with film thickness, together with a gradual decrease in the average vertical fraction is qualitatively in agreement with our previous study on lamellar BCP films coated on silica nanoparticles.³¹ When the film thickness is commensurate with lamellae repeat period ($h \approx nL_0$ or $h \approx (n + 1/2)L_0$), the lamellae preferably orient horizontally whereas for the other noncommensurate film thickness values (particularly $h < 40$ nm and around 56 nm), vertically oriented lamellae were observed over large areas, as alternate to parallel lamellae with unfavorable energetics associated with islands and holes formation.

Visual analysis of Figure 3 shows that as γ_s is increased, the areas of vertical orientation for $h < 40$ nm decreased drastically, so that $\gamma_s = 29$ mJ/m² is most effective in vertically orienting the PS–PMMA lamellae on the $R_{\text{rms}} = 5.1$ nm rough xerogel surface. Even for $h > 40$ nm, e.g. for fixed $h = 58$ nm, with increase in γ_s from 29 to 53 mJ/m² quantitative analysis of the areas with vertical orientation showed that they decreased gradually from 100% to 5%. These results are different from smooth silicon surfaces coated with a neutral brush layer or a UVO–SAM layer where the neutral value of $\gamma_s = 37$ – 40 mJ/m² best result in vertically oriented PS–PMMA cylinders and lamellae. However, it appears that with a modest roughness of $R_{\text{rms}} = 5.1$ nm on the rough xerogel surface, there is a drastic shift of the neutral value to significantly lower surface energy values, $\gamma_{s\text{-neutral}} \sim 29$ mJ/m². Note however that $R_{\text{rms}} = 5.1$ nm is 1/7th of BCP domain spacing of 35 nm, so even a small perturbation of R seems to shift the landscape for neutral surface energy regime. This idea needs to be further explored in future experimental and theoretical models. Given this shifted neutral surface energy value, it is not surprising that a decrease in the vertical orientation is expected with increasing surface energy of the substrate γ_s from 29 to 53 mJ/m² because of increased preferential wetting of the SiO₂ surface by PMMA inducing horizontal orientation in lamellae.

We do not make any correction to the surface energies measured by traditional polar and nonpolar solvent contact angle method on the xerogel surfaces because previous literature shows that only for surface with roughness amplitudes much greater than 500 nm, there is a possibility of trapped air cushion underneath the liquid droplets.^{39–41} Therefore, we discard the possibility of Cassie regime of droplet wetting. For a Wenzel drop, the difference is apparent; i.e., θ_W is Wenzel contact angle measured by experiments for a liquid drop on surface with roughness R and the ideal Young contact angle θ_Y are related as per the equation⁴²

$$\cos \theta_W = R \cos \theta_Y$$

Using the ideal contact angle values in the above equation leads to a very small correction in surface energy values. Our preliminary calculations show that for the rough surfaces used in the present studies the correction to the measured contact angle would lead to change of ± 1 mJ/m² in the reported surface energy values. Even with a projected 2/3 contact area for a Cassie liquid drop, the correction to the measured contact angle would lead to a change of ± 2 mJ/m² in measured surface

energy. For the xerogel surfaces studied here, the projected contact area is much greater than 2/3 fraction.

Another interesting comparison comes from our results on lamellar PS-PMMA BCP films on SiO₂ nanoparticle layers from the previous study,³¹ where the decrease in lamellar fraction was shown to be far more gradual than the sharp horizontal flipping of lamellae for thinner films (≤ 40 nm) observed here when γ_s increased by only 9 mJ/m², i.e., from 29 to 38 mJ/m². As lamellae orientation studied using AFM is limited to the surface of the films, we employed rotational small-angle neutron scattering (R-SANS) to measure the average surface as well as subsurface ordering of lamellae integrating over the entire thickness of the film where the scattering intensity is accumulated as a function of sample rotation angle. The sample rotation also enables measurement of the population of lamellae oriented at different angles to generate 3-D volumetric scattering data. Figure 3c(1–3) shows RSANS data for BCP film coated on $\gamma_s = 29$ mJ/m² and Figure 3d(1–3) for $\gamma_s = 38$ mJ/m² (spots marked as c and d in Figure 3b at 40 nm). Figures 3(c1) and 3(d1) show 2D slices of 3D reciprocal-space maps, generated by rotating the sample in the neutron beam, and Figures 3(c2) and 3(d2) show corresponding fits that are in excellent agreement. This nontrivial fit to data is accomplished using a model developed previously consisting of a mixture of parallel and perpendicular lamellae where their relative ratios are varied to best fit the data.³¹ This also shows that the AFM surface orientation observations were well supported by the R-SANS experiments. In these figures, the in-plane scattering vector (Q_x or Q_y) is along the horizontal axis, and Q_z , the vector pointing normal to the film thickness, is along the vertical axis. Figures 3(c3) and 3(d3) show orientational distribution of lamellae as a function of tilt angle (0° denotes vertically oriented lamellae, whereas $\pm 90^\circ$ denotes horizontally oriented lamellae) for $\gamma_s = 29$ and 38 mJ/m², respectively. For, $\gamma_s = 29$ mJ/m² and $h = 40$ nm, the AFM shows almost 100% area of vertically oriented lamellae as shown schematically, and reciprocal-space maps generated from R-SANS shown in Figures 3b(1–2) show a bright peak around 0.16 nm^{-1} , indicating strong scattering from vertically oriented lamellae in the film. The intensity at low Q in the RSANS data is diffuse scattering interrupted by the beam stop which is attributed to the disordered xerogel material, which has a broad distribution of pore size and pore shape. It should also be noted that vertical lamellae population (central peak at around 0°) exhibits a larger angular spread than the horizontal population (side peaks at -90° and $+90^\circ$) for the lamellar orientation, as seen from Figure 3(c3). However, the horizontal population has a larger spread than lamellar BCP coated on Xero-R0.5 nm (Figure 2) or other flat substrates like Si wafer, indicating that the substrate roughness even disrupts the horizontal state. This drastic change in orientation of lamellae from predominantly vertical to horizontal for a change in γ_s from 29 to 38 mJ/m² suggests a strong “pore templating” of lamellae negates the roughness effects of the substrate. It appears that in the small-thickness regime ($h < 40$ nm), the relatively large pores of the xerogel substrate have a dominant effect in controlling the BCP order. In particular, the lamellae stack parallel to substrate plane by maintaining orthogonal orientation with respect to the near vertical pore walls in the vicinity of the top xerogel surface. This orientation is similar to previous work on poly(styrene-*b*-butadiene) lamellar BCP confinement in cylindrical pores.⁴³ As the xerogel pores are about 30 nm deep, this effect is more pronounced for BCP film thickness smaller than 40 nm.

However, as the thickness of the film is increased and exceeds the pore depth, the lamellae tend to orient parallel and vertical in an oscillatory manner at commensurate-incommensurate thicknesses conditions due to the nanoscale roughness. At these thicknesses, it is conceivable that a conformal wetting layer of $L_0/4$ thickness is forming at the substrate interface. However, we observed that for films above this thickness, lamellae orient vertically at incommensurate thicknesses so as to lower the energy penalty due to both polymer block bending and increased interfacial area required for blocks to conformally coat the rough substrate. At lower surface energy, this pore templating effect becomes less effective than the effects of roughness and the neutrality of the surface toward the blocks. From the color band spectra, it also appears that the region of vertical orientation is shifting toward higher thickness to around 60 nm, but considering the uncertainty in the measurement of exact thickness of the film by AFM, it is not possible to speculate further on the shift and its cause.

30 nm Rough Xerogel Substrate. Figure 4 shows orientation map for BCP films coated on Xero-R30 nm

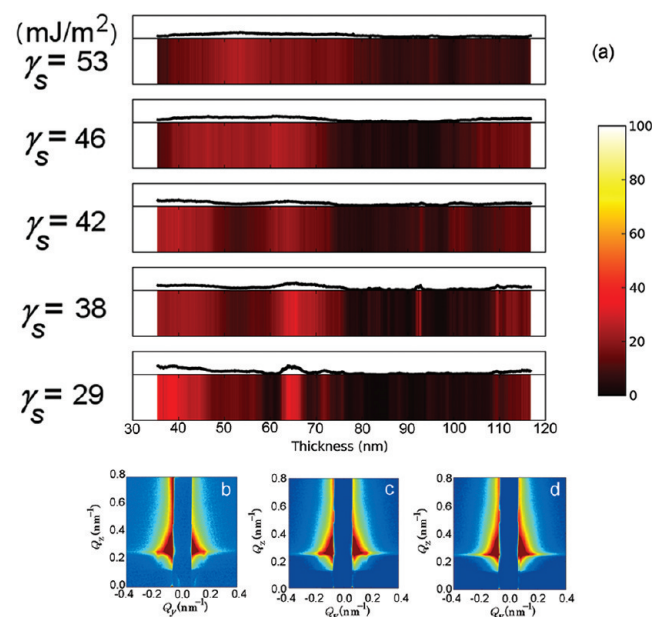


Figure 4. (a) Color bands show percentile perpendicular lamellae distribution as a function of xerogel surface energy (γ_s) and film thickness for PS-PMMA films coated on Xero-R30 nm. GISAXS data recorded at X-ray incidence angle of 0.2° for (b) 40, (c) 65, and (d) 80 nm thick films coated on substrate with $\gamma_s = 29$ mJ/m². The small percentage of vertical lamellae detected by GISAXS (red dot contours around $Q_y = -0.2\text{ nm}^{-1}$ and $+0.2\text{ nm}^{-1}$ in (b) and (c) disappeared in (d) with increase in film thickness confirming AFM observations.

substrate which has $R_{\text{rms}} = 30.4$ nm and $D_f = 2.4$. It was observed that as substrate roughness increased to 30.4 nm, the area of 100% vertically oriented lamellae was not observed at all even at lower surface energy $\gamma_s = 29$ mJ/m², irrespective of the thickness even though this substrate exhibited highest roughness compared to all the other substrates used in this study. Also with $D_f = 2.4$, the fractal dimension of the substrate is higher than all but for the nanoparticle SNP80-R5 nm substrate from ref 31 among the substrates compared here. This point will be discussed later in more detail in connection with Figure 7. However, comparing Figures 3b and 4a, it is clear that less than 10% areas with vertical lamellae were obtained for Xero-

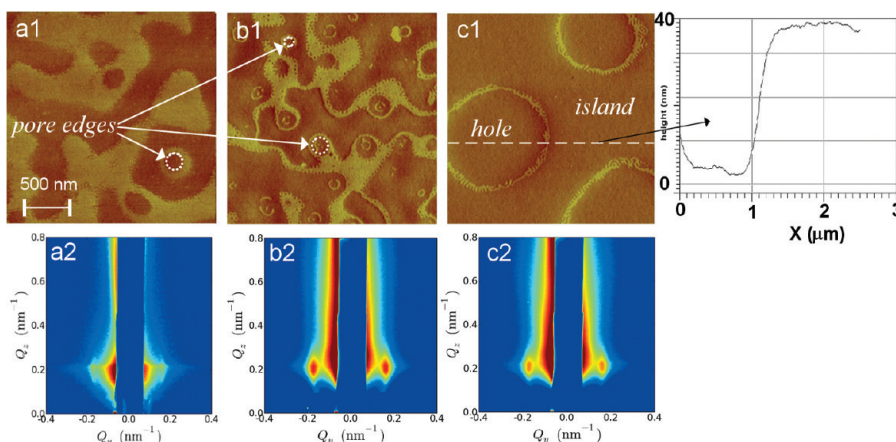


Figure 5. Top row (a1–c1): AFM phase images of PS–PMMA films (scale bar: 500 nm for all AFM images). Corresponding GISAXS images recorded at X-ray incidence angle of 0.15° are shown in the bottom row (a2–c2). Inset shows AFM topography cross section at the dashed line in c1 (Y-axis scale 0–40 nm). The AFM phase images show effect of substrate porosity and film thickness on the microphase separation of BCP. The circular patterns indicate strong influence of pore geometry, while the other patterns show a complex distribution of parallel and perpendicular lamellae due to nonuniform film thickness. (a1, a2) 40 nm film coated on Xero-R5 nm with $\gamma_s = 38 \text{ mJ/m}^2$. GISAXS confirms almost negligible presence of vertical lamellae. (b1, b2) 40 nm film on Xero-R30 nm with $\gamma_s = 29 \text{ mJ/m}^2$. Red contours around $Q_y = -0.2 \text{ nm}^{-1}$ and $+0.2 \text{ nm}^{-1}$ in the GISAXS data show presence of perpendicular lamellae that decreased significantly with increase in the film thickness as shown in (c1, c2), 60 nm thick film on Xero-R30 nm with $\gamma_s = 29 \text{ mJ/m}^2$.

R5 nm, for film thicknesses below 60 nm and $\gamma_s \geq 38 \text{ mJ/m}^2$, whereas for films coated on Xero-R30 nm about vertically oriented lamellae were obtained over $\sim 25\%$ areas for 40 and 60 nm thickness, even for γ_s as high as 53 mJ/m^2 . However, the vertical orientation was never close to complete coverage at any thickness and surface energy combination. In fact, for all other thicknesses, $<10\%$ area of the film had vertically oriented lamellae.

Considering the higher $R_{\text{rms}} = 30 \text{ nm}$ and porosity of the substrate, these results are consistent with the pore-wetting argument presented earlier. To understand the subsurface orientation of the lamellae, we used Grazing-incidence small-angle X-ray scattering (GISAXS). By changing the angle of X-ray incidence, lamellar orientation was studied along the depth of the film. Figure 4b–d shows GISAXS results obtained at X-ray incidence angle of 0.2° for (b) 40, (c) 65, and (d) 80 nm thick films coated on a substrate with $\gamma_s = 29 \text{ mJ/m}^2$. As seen from the circular red colored contours around $Q_y = -0.2$ and 0.2 nm^{-1} , a small percentage of vertical lamellae are present in (b) and (c) which disappeared with increase in film thickness in (d), thus confirming that the surface orientation observations from AFM persists even inside the film. It should be noted that the Q values of the first-order peak in RSANS presented in earlier Figures 2 and 3 and those from GISAXS match up well. In RSANS, the peak appears at $Q \sim 0.18 \text{ nm}^{-1}$, whereas in GISAXS, the in-plane periodicity occurs at same $Q_y \sim 0.18 \text{ nm}^{-1}$. The peak maximum in the Q_z direction in GISAXS is offset by the reflection-mode geometry. So with the increase in film thickness the small but robust vertical population disappears as confirmed by AFM measurements on surface and by GISAXS throughout the film. The surprising absence of higher percentage of vertically oriented lamellae on Xero-R30 nm substrates can be explained as follows. Since these substrates had deeper pores (up to 100 nm deep) than any of the other substrates, it is possible that the confinement induced ordering of the BCP inside the pores of the substrate had a templating effect on its orientation in the film up to the free surface. We attribute the diffuse low- Q scattering (seen on either side of the beam stop in the GISAXS images) to the

porous xerogel substrate. Because of the extremely broad distribution in pore size, the scattering from these structures does not appear as a distinct structural peak and instead contributes to the diffuse scattering. The effect of pores on the orientation of BCP phases is discussed in more detail below.

Figure 5 shows the effect of xerogel pores on PS–PMMA BCP orientation on a relatively hydrophilic ($\gamma_s = 38 \text{ mJ/m}^2$), Xero-R5 nm substrate ($h = 40 \text{ nm}$), as well as on hydrophobic ($\gamma_s = 29 \text{ mJ/m}^2$) Xero-R30 nm substrates ($h = 40$ and 60 nm).

AFM phase images of the microphase-separated films are shown in the top row (Figure 5, a1–c1). GISAXS was again used to corroborate the AFM phase data (Figure 5, a2–c2). The X-ray incidence angle in this case was kept at 0.15° so that X-rays scattering mainly arises from the top layer of the BCP film. As discussed above, it was observed that as γ_s decreased from 29 mJ/m^2 , orientation of BCP films coated on Xero-R5 nm declined drastically from almost 100% to less than 10% area showing vertically oriented lamellae at all thicknesses below 40 nm. As seen in Figure 5(a1), phase scans of the top surface of the film show polymer blocks assembled in a ringlike formation with the ring diameters corresponding to the pore diameters with only a small area fraction of perpendicularly oriented lamellae found predominantly at the edge of these rings. GISAXS of this film shown in Figure 5(a2) also does not show any significant signal of vertical lamellae. Similar ringlike lamellae were also observed for BCP films coated on Xero-R30 nm substrates as shown in Figure 5(b1) for $h = 40 \text{ nm}$ and $\gamma_s = 29 \text{ mJ/m}^2$. However, here the pore effect is more pronounced with sharper concentric rings composed of almost only one block length. Therefore, these rings give rise to relatively strong scattering intensity in GISAXS, confirming a vertical orientation of lamellae at the surface. However, as the BCP film thickness increased to 60 nm (Figure 5(c1)), the diameter of the ringlike structures increased and some perpendicular orientation was observed only on the edges of these rings. Here, these rings are most likely a result of island and hole formation with island height $\sim 40 \text{ nm}$ (AFM topographic cross section of the film is shown in the Figure 5, inset) as the ring diameter was much bigger than the substrate pore diameter. Also, GISAXS showed

(Figure 5(c2)) a very weak scattering signal from vertically oriented lamellae, indicating a predominantly horizontal orientation of lamellae that is consistent with the hole and island formation mechanism. These observations are also in accord entirely with the AFM results showing that the vertical orientation is energetically favorable in thinner films. As a further check, the X-ray incidence angle was increased to 0.2° , which probes the entire film thickness. In this case, the scattering corresponding to vertically oriented lamellae decreased significantly (see Supporting Information). This observation indicates that the vertical orientation is localized at the air interface (or at the top edges of the pores) and the lamellae stack parallel inside the pores. As the pores of Xero-R30 nm are much deeper (up to 100 nm), the parallel stacking of the lamellae inside the pores is more prominent for the BCP films coated on these substrates. Therefore, it appears that only the incommensurate thick part of the BCP forms the ringlike structures, whereas most of the lamellae lie parallel to the substrate. Control over the sizes and shapes of these structures could be very useful for nanopatterning applications.

5 nm Rough Silica NP Substrate. The case of BCP films coated on monodisperse (20 nm) nanoparticle layered substrate SNP80-R5 nm shown in Figure 6 makes an interesting case for comparison with xerogel substrates.

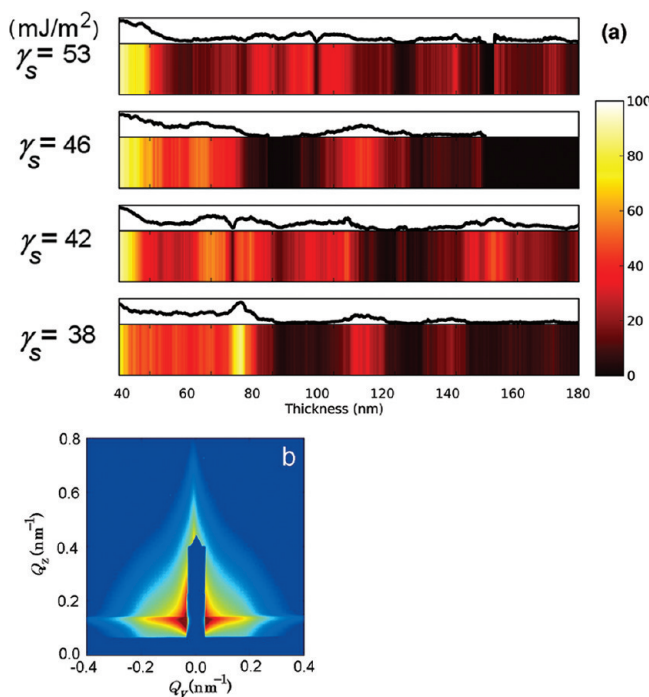


Figure 6. (a) Color bands show percentile perpendicular lamellae distribution as a function of xerogel surface energy (γ_s) and film thickness for PS-PMMA films coated on SNP80-R5 nm. (b) A typical GISAXS contour map for $\gamma_s = 38$ mJ/m² and film thickness of 40 nm.

Areas with 100% perpendicularly oriented lamellae were observed at broader thicknesses range from <40 nm and also from 65 to 70 nm with $\gamma_s = 38$ mJ/m². Even for intermediate thickness values between these two peaks, the lamellae still show good degree of vertical orientation (30–60%). Observe that the smooth surface neutral $\gamma_s = 38$ mJ/m² is recovered in this coated nanoparticle substrate system. In the thickness range of 70–110 nm, most of the lamellae orient horizontal and around 110 nm thickness reached another incommensurate

regime where areas of 25–30% vertically oriented lamellae are observed. The trend continued over the entire surface energy, with little variation in the thickness and area fraction of vertical lamellae. The range shifts observed in the areas of perpendicular orientation bands as a function of thickness and γ_s values are mainly because of the inaccuracies arising from the exact thickness measurements over entire range of the BCP film coated on rough xerogel and SiO₂ nanoparticle substrates using existing thickness measurements techniques. The rough polymer–substrate interface comprised of disordered and fractal nanoparticle layer also leads to a significant diffuse low- q scattering in GISAXS measurements as seen in Figure 6b, overwhelming any signal of vertical lamellae. This scattering likely arises from the disordered and fractal nanoparticle layer, which inherently includes structure across a distribution of size scales, leading to the diffuse scattering. However, it can be surmised that surface characteristics of monodisperse 20 nm size nanoparticle layer of SNP80-R5 nm are more suitable for obtaining vertically oriented lamellae in PS-PMMA films from the AFM results over a broader range of the surface energies. Interestingly, even though the R_{rms} of the SNP80-R5 nm substrate is only 5.2 nm (almost equal to Xero-R5 nm), this substrate treatment proved to be superior for producing vertically oriented lamellae over a wide range of BCP film thickness and surface energy. As the R_{rms} of the SNP80-R5 nm substrate is only 5.2 nm (almost equal to Xero-R5 nm), and the range of surface energies is similar to that of all other substrates, this dramatic improvement in the vertical orientation of lamellae must be a result of combination of its higher fractal dimension ($D_f = 2.5$) and nonporous nature of the SNP80-R5 nm substrate. In other words, this type of substrate achieves most robust vertical orientation which is rather insensitive to the film and substrate characteristics and is more tolerant of patchy nanoparticle defects.³¹

It is clear from these experiments that roughness (R_{rms} amplitude) is not the only isolated parameter to study orientation of BCP films and effect of fractal dimension of the substrate also must be taken into account. To understand of the combinatorial effect of R_{rms} and D_f on vertical orientation of lamellae, we compared results of our experiments described here on PS-PMMA BCP films on silica nanoparticle layers and xerogel substrates with results from our previously study³¹ on silica nanoparticle substrates presented in Figure 7. The top row of the figure shows a schematic of PS-PMMA lamellae (with $L_0 = 35$ nm) orientation on surfaces with a plot of fractal dimension vs R_{rms} . The data point corresponding to $D_f = 2.65$ and $R_{\text{rms}} = 11$ nm is taken from the above-mentioned reference.³¹ As seen from the figure, vertical orientation of lamellae is not linearly dependent on R_{rms} . However, when the rms roughness of the substrate was well below L_0 , vertical lamellar orientation improved drastically with an increase in D_f . From these results we propose that small roughness ($\leq L_0$) is a necessary but not a sufficient condition for better vertical orientation of lamellae in BCP films. In general, fractal dimensions of the substrate appear to correlate much better with the orientational order of BCP films, and our current experiments on PS-PMMA lamellar BCP films with $L_0 = 35$ nm serve as experimental validation that high fractal dimension ($D_f \geq 2.5$) leads to better vertical orientation. The effect of fractal dimension on orientation of BCP can be explained as follows. The BCP blocks would have to follow a very torturous path if they have to conformally coat (i.e., horizontally oriented lamellae) such a surface as shown in Figure 7c(ii) as compared

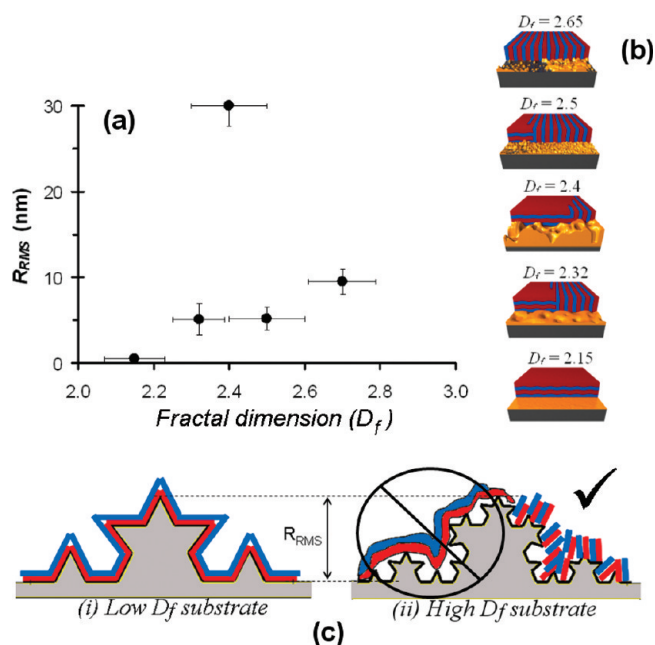


Figure 7. (a) Plot of fractal dimension (D_f) vs root-mean-square roughness (R_{rms}) of the substrates used in the present study and substrate with $D_f = 2.65$ from ref 31. (b) Schematics show the distribution of parallel and perpendicular microphase-separated BCP lamellae for a film thickness $\approx L_0$ coated on a hydrophobic substrate ($\gamma_s = 29$ mJ/m²) and the surface features of the substrate corresponding to each of the data point. (c) Schematic comparing lamellae orientation on (i) low and (ii) high D_f substrate with similar R_{rms} .

to a surface with smaller fractal dimension with almost similar roughness Figure 7c(i). As a case point, comparison of BCP orientation on Xero-R5 nm ($D_f = 2.32$) and SNP80-R5 nm ($D_f = 2.5$) clearly showed that even though these two substrates have nearly identical $R_{rms} \approx 5$ nm, the higher fractal dimension of SNP80-R5 nm resulted in more areas of higher percentage of vertically oriented lamellae over larger thickness and surface energy span. As shown in Figure 7, our results indicate that the conformal lamellae orientation (i.e., parallel to the substrate) is less probable on a rough but higher D_f substrate.

The multiscale features of fractal surfaces imply that a wide range of undulation length scales (both in-plane and normal) are present, so that the domain spacing or characteristic wavelength of the BCPs cannot couple to the roughness present on fractal surfaces. The flexing of BCP interface at several length scales and amplitude drastically increases the interfacial energy penalty for the blocks. Alternatively, vertical orientation would be preferred. As a further measure to understand effect of fractal dimension on BCP orientation, we assumed a monolayer of BCP behaves like Alexander–deGennes brush and compared free energy expressions of the brush in both parallel and perpendicular orientations in various asymptotic regimes. We were able to qualitatively show that perpendicular orientation is the equilibrium state on higher fractal dimension surfaces for these brushes.⁴⁴ However, synergistic effect of fractal dimension, roughness, and surface energy must be considered for estimating final desired orientation of BCP films. The fractal dimensions reported here were measured by AFM; however, it is known that D_f measurements obtained by AFM are subject to some caveats.⁴⁵ In view of the fact that all physical realizations of a fractal

display self-similarity (a condition for a mathematical fractal object) within a window of length scales, the interpretation of results based on D_f should be done carefully. Future experiments on BCP films with different lamellar period to test applicability of our results on BCP films with different molecular weights (lamellar periods) are planned.

4. CONCLUSIONS

We demonstrated a novel and versatile method to produce robust inorganic substrates with different fractal rough characteristics as well as surface energy by tuning various sol–gel processing parameters and UVO exposure of the substrates. It was observed that the rms roughness of the xerogel substrates can be increased from 0.5 to ≈ 30 nm by increasing base catalyst concentration from 0.1 to 0.2 along with increase in sol aging time. It was also observed that a robust vertical orientation in lamellar microphase-separated PS–PMMA BCP thin films can be achieved on these fractally rough substrates. The lamellae orientation was studied as a function of substrate surface energy and film thickness. The microphases orient alternatively perpendicular and parallel as a function of thickness, with a separation of $\sim L_0$ between adjacent vertical regions demonstrating their dependence on the BCP ordering process. The lamellae orient perpendicular and parallel at incommensurate and commensurate thicknesses, respectively. It was observed that by increasing the fractal dimension (D_f) of the substrate, the BCP microphases can be forced to orient vertically over a large area fraction and over a wide range of film thickness and substrate surface energies. In particular, for $D_f > 2.4$, 100% vertically oriented lamellae were obtained for incommensurate thicknesses of 35–40 nm and 60–70 nm for a BCP films coated on a near-neutral rough surface. The vertical orientation was even maintained for more hydrophilic surfaces, even for the BCP films twice as thick as the lamellar period ($\approx 2L_0$). As expected, the orienting effect of the substrate disappeared at higher thicknesses due to preferential surface wetting effects of BCP. The moderate size pores in the xerogel substrates with $R_{rms} = 5.1$ nm were found affect the microphase orientation for surfaces with all γ_s values except 29 mJ/m². The pore templating effect was more pronounced on a highly rough surface with $R_{rms} = 30$ nm, where no area with 100% vertical lamellae was obtained for any surface energy. These results suggest that different surface preparations which have the same average roughness may nevertheless lead to different kinds of ordering. In particular these experimental results point to an important role of fractal characteristics of the substrate for obtaining vertically oriented lamellae, which are not controlled by the substrate roughness alone. In fact, small roughness is a necessary, but not sufficient, condition in the control of BCP film orientation and in general, higher percentage of vertical orientation can be achieved on a rough substrate with a higher fractal dimension (D_f), at least in the case of PS–PMMA lamellar BCP films.

Use of sol–gel processing and nanoparticle coating allows preparing large area substrates with different roughness characteristics and these methods may provide inexpensive and industrially viable alternatives to the other competing techniques such as lithographically processed physicochemically patterned substrates. Moreover, a variety of industrial surfaces are inherently rough; thus, these results could be instrumental in helping select appropriate existing materials which, with little to no modification, could act as ideal substrates for controlling the BCP order.

■ ASSOCIATED CONTENT

■ Supporting Information

Additional GISAXS images of BCP films coated on xerogel substrate at and above critical X-ray incidence angle. This material is available free of charge via the Internet at <http://pubs.acs.org>.

■ AUTHOR INFORMATION

Corresponding Author

*Ph +1-330-972-8324; e-mail alamgir@uakron.edu.

Notes

The authors declare no competing financial interest.

■ ACKNOWLEDGMENTS

A. Karim acknowledges U.S. Department of Energy grant # DE SC0005 364 for partial support of this work. We acknowledge Joseph Strzalka for help with X-ray scattering measurements. Use of the Advanced Photon Source was supported by the U.S. Department of Energy, Office of Science, Office of Basic Energy Science, under Contract W-31-109-Eng-38. We acknowledge the support of the National Institute of Standards and Technology, U.S. Department of Commerce, in providing the neutron research facilities used in this work. Work carried out at the Center for Functional Nanomaterials, Brookhaven National Laboratory, was supported by the U.S. Department of Energy, Office of Basic Energy Sciences, under Contract DE-AC02-98CH10886. A.S. and M.M.K. acknowledge support from IUSSTF, New Delhi, and A.S. from DST Unit on Nanosciences at IITK and a DST IRHPA grant.

■ REFERENCES

- (1) Tuteja, A.; Choi, W.; Ma, M.; Mabry, J. M.; Mazzella, S. A.; Rutledge, G. C.; McKinley, G. H.; Cohen, R. E. *Science* **2007**, *318*, 1618–22.
- (2) Furstner, R.; Barthlott, W.; Neinhuis, C.; Walzel, P. *Langmuir* **2005**, *21*, 956–961.
- (3) Rao, A. V.; Kulkarni, M. M.; Amalnerkar, D. P.; Seth, T. J. *Non-Cryst. Solids* **2003**, *330*, 187–195.
- (4) Volodin, P.; Kondyurin, A. *J. Phys. D: Appl. Phys.* **2008**, *41*, 065307.
- (5) Mirantsev, L. V.; Zakharov, A. V.; Korsakov, V. G. *Phys. Solid State* **1999**, *41*, 306–312.
- (6) Chow, T. S. *Phys. Rev. Lett.* **2001**, *86*, 4592–4595.
- (7) Gentile, F.; Tirinato, L.; Battista, E.; Causa, F.; Liberale, C.; Fabrizio, E. M.; di Decuzzi, P. *Biomaterials* **2010**, *31*, 7205–7212.
- (8) Kim, S. O.; Solak, H. H.; Stoykovich, M. P.; Ferrier, N. J.; Pablo, J. J. De; Nealey, P. F. *Nature* **2003**, *424*, 411–4.
- (9) Hawker, C.; Russell, T. P. *MRS Bull.* **2005**, *30*, 952–966.
- (10) Albert, J. N. L.; Epps, T. H., III. *Mater. Today* **2010**, *13*, 24–33.
- (11) Moore, G. E. *Proc. SPIE* **1995**, *2437*, 2–17.
- (12) Guo, J. Z. Y.; Novembre, A.; Marchman, H.; Abate, J.; Frackowiak, J.; Tomes, D.; Timko, A.; Celler, G. K. *Proc. SPIE* **1995**, *2437*, 86–93.
- (13) Li, M.; Ober, C. K. *Mater. Today* **2006**, *9*, 30–39.
- (14) Gates, B. D.; Xu, Q.; Stewart, M.; Ryan, D.; Willson, C. G.; Whitesides, G. M. *Chem. Rev.* **2005**, *105*, 1171–96.
- (15) Matsen, M. W.; Bates, F. S. *Macromolecules* **1996**, *29*, 1091–1098.
- (16) Park, S.; Lee, D. H.; Xu, J.; Kim, B.; Hong, S. W.; Jeong, U.; Xu, T.; Russell, T. P. *Science* **2009**, *323*, 1030–3.
- (17) Asakawa, K.; Hiraoka, T.; Hieda, H.; Sakurai, M.; Kamata, Y.; Naito, K. *J. Photopolym. Sci. Technol.* **2002**, *15*, 465–470.
- (18) Fasolka, M. J.; Mayes, A. M. *Annu. Rev. Mater. Res.* **2001**, *31*, 323–355.
- (19) Russell, T. P.; Coulon, G.; Deline, V. R.; Miller, D. C. *Macromolecules* **1989**, *22*, 4600–4606.
- (20) Tang, C.; Lennon, E. M.; Fredrickson, G. H.; Kramer, E. J.; Hawker, C. J. *Science* **2008**, *322*, 429–32.
- (21) Kim, D. H.; Lin, Z.; Kim, H.-C.; Jeong, U.; Russell, T. P. *Adv. Mater.* **2003**, *15*, 811–814.
- (22) Tada, Y.; Akasaka, S.; Yoshida, H.; Hasegawa, H.; Dobisz, E.; Kercher, D.; Takenaka, M. *Macromolecules* **2008**, *41*, 9267–9276.
- (23) Yang, X. M.; Peters, R. D.; Nealey, P. F.; Solak, H. H.; Cerrina, F. *Macromolecules* **2000**, *33*, 9575–9582.
- (24) Bang, J.; Bae, J.; Löwenhielm, P.; Spiessberger, C.; Given-Beck, S. A.; Russell, T. P.; Hawker, C. *Adv. Mater.* **2007**, *19*, 4552–4557.
- (25) Huang, E.; Rockford, L.; Russell, T. P.; Hawker, C. J. *Nature* **1998**, *395*, 757–758.
- (26) Lin, Y.; Böker, A.; He, J.; Sill, K.; Xiang, H.; Abetz, C.; Li, X.; Wang, J.; Emrick, T.; Long, S.; Wang, Q.; Balazs, A.; Russell, T. P. *Nature* **2005**, *434*, 55–59.
- (27) Hu, S.; Brittain, W. J.; Jacobson, S.; Balazs, A. *Eur. Polym. J.* **2006**, *42*, 2045–2052.
- (28) Sivaniah, E.; Hayashi, Y.; Matsubara, S.; Kiyono, S.; Hashimoto, T.; Fukunaga, K.; Kramer, E. J.; Mates, T. *Macromolecules* **2005**, *38*, 1837–1849.
- (29) Son, J. G.; Bulliard, X.; Kang, H.; Nealey, P. F.; Char, K. *Adv. Mater.* **2008**, *20*, 3643–3648.
- (30) Kulkarni, M. M.; Bandyopadhyaya, R.; Bhattacharya, B.; Sharma, A. *Acta Mater.* **2006**, *54*, 5231–5240.
- (31) Yager, K. G.; Berry, B. C.; Page, K.; Patton, D.; Karim, A.; Amis, E. J. *Soft Matter* **2009**, *5*, 622.
- (32) Berry, B. C.; Stafford, C. M.; Pandya, M.; Lucas, L. A.; Karim, A.; Fasolka, M. J. *Rev. Sci. Instrum.* **2007**, *78*, 072202.
- (33) Owens, D. K.; Wendt, R. C. *J. Appl. Polym. Sci.* **1969**, *13*, 1741–1747.
- (34) Stafford, C. M.; Roskov, K. E.; Epps, T. H.; Fasolka, M. J. *Rev. Sci. Instrum.* **2006**, *77*, 023908.
- (35) Brinker, C. J. *J. Non-Cryst. Solids* **1988**, *100*, 31–50.
- (36) Fasolka, M. J.; Harris, D. J.; Mayes, A. M.; Yoon, M.; Mochrie, S. G. *J. Phys. Rev. Lett.* **1997**, *79*, 3018–3021.
- (37) Rao, A. V.; Kulkarni, M. M.; Seth, T.; Amalnerkar, D. P. *Appl. Surf. Sci.* **2003**, *206*, 262–270.
- (38) Roberson, S.; Fahey, A.; Sehgal, A.; Karim, A. *Appl. Surf. Sci.* **2002**, *200*, 150–164.
- (39) Marmur, A.; Bittoun, E. *Langmuir* **2009**, *25*, 1277–81.
- (40) Ran, C.; Ding, G.; Liu, W.; Deng, Y.; Hou, W. *Langmuir* **2008**, *24*, 9952–5.
- (41) Vrancken, R. J.; Kusumaatmaja, H.; Hermans, K.; Prenen, A. M.; Pierre-Louis, O.; Bastiaansen, C. W. M.; Broer, D. J. *Langmuir* **2010**, *26*, 3335–41.
- (42) Marmur, A. *Langmuir* **2003**, *19*, 8343–8348.
- (43) Shin, K.; Xiang, H.; Moon, S. I.; Kim, T.; McCarthy, T. J.; Russell, T. P. *Science* **2004**, *306*, 76.
- (44) Ranjan, A.; Kulkarni, M.; Karim, A.; Sharma, A. *J. Chem. Phys.* **2012**, *136*, 094903.
- (45) Douketis, C.; Wang, Z.; Haslett, T. L.; Moskovits, M. *Phys. Rev. B* **1995**, *51*, 11022–11031.